ACS APPLIED ELECTRONIC MATERIALS

pubs.acs.org/acsaelm Article

Evolution of Magnetism Induced by K^+/La^{3+} Implantations in Double Perovskite Ba_2MnTeO_6

Haipeng You, Yixiao Chen, Yue Li, Jun Chen,* Xiyu Chen, Meifeng Liu, Shuai Dong, and Jin Peng*

Cite This: *ACS Appl. Electron. Mater.* 2024, 6, 4903−4911 Read Online

ACCESS | Metrics & More | Article Recommendations | Supporting Information

ABSTRACT: *B*-site rock salt type ordered double perovskites with general formula $A_2B'B''X_6$ have attracted a variety of attention due to remarkable magnetic properties and potential applications in spintronics. Here we report the structural, magnetic, and electronic properties of polycrystalline compounds Ba_2MnTeO_6 and $(Ba_{0.9}X_{0.1})_2MnTeO_6$ (X = K/La) by powder X-ray diffraction, magnetic susceptibility measurements, specific heat measurements, and X-ray photoelectron spectroscopy. Ba_2MnTeO_6 is antiferromagnetically ordered below 20 K. Density functional theory calculations show that Ba_2MnTeO_6 prefers type III antiferromagnetic order with a dominant antiferromagnetic nearest-neighbor exchange and a weak ferromagnetic next-nearest-neighbor exchange. Our Monte Carlo simulations lead to a transition temperature of 28 K, consistent with the experimental results. Upon K^+/La^{3+} cations' implantation on Ba sites, while $(Ba_{0.9}K_{0.1})_2MnTeO_6$ orders antiferromagnetically at 20 K, $(Ba_{0.9}La_{0.1})_2MnTeO_6$ exhibits superparamagnetism below room temperature, which may originate from oxygen ion adsorptions. These findings reveal the modulation of magnetism for Ba_2MnTeO_6, which may hint at potential applications of double perovskites in magnetic devices.

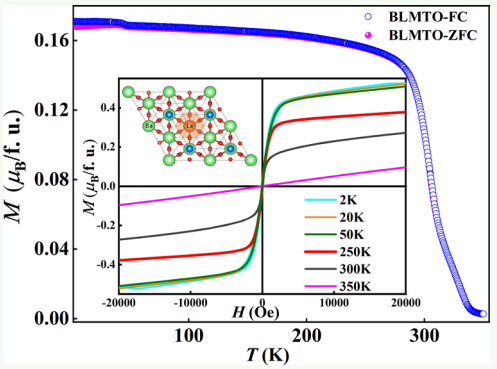

KEYWORDS: *Double perovskites, Density functional theory, Monte Carlo simulation, Superparamagnetism, Oxygen adsorption*

INTRODUCTION

Crystalline perovskite compounds are among the most intensively studied materials in solid-state physics and chemistry due to their superior magnetic and electronic properties, which are widely used in microelectronics, spintronics, sensor devices, etc.[1−7] Nevertheless, the applications of perovskites are limited by their drawbacks, such as material instability and low functioning temperature. Thus, exploring more versatile perovskites is crucial for fundamental science and device applications.

Double perovskites with *B*-site cations ordered in the rock salt type ($A_2B'B''X_6$) attracted considerable attention recently;[8−12] here *A* represents a divalent cation, *B*′ denotes a 3*d* transition metal ion, *B*″ signifies a hexavalent ion, and *X* represents chalcogen ions. The 3*d* transition metal ions form a triangular lattice, leading to exotic magnetic properties. Such systems also possess giant magnetoresistive and dielectric properties, which bring more possibilities for high integrability of spintronic devices. As early as 1997, a battery of tellurate oxides, including Ba_2MnTeO_6 (BMTO) and Pb_2MnTeO_6, were synthesized and reported by Wulff et al.[13] Their crystal structures were also determined via X-ray investigations. Lately, Pb_2MnTeO_6 was investigated by Retuerto et al.,[14] which undergoes a phase transition from *I*2/*m* to the *C*2/*c* space group. The ground state of Pb_2MnTeO_6 is an antipolar antiferromagnet with a lower Néel temperature (20 K). This work has also motivated more researchers to pursue high-performance double tellurates.

Recently, the crystal structure and electronic and magnetic properties of BMTO have been further investigated by several groups. Mustonen et al.[15] confirmed that it has a cubic *Fm*-3*m* structure with lattice parameter a = 8.206 Å and orders antiferromagnetically below $T_N \sim 20$ K. Subsequently, Li et al. reported a triangular phase with the *R*-3*m* space group, a stripe-type antiferromagnetic (AFM) order with a Néel temperature of $T_N \sim 20$ K, and a propagation vector k = (0.5, 0.5, 0).[16] Khatua et al. also found BMTO crystallized in trigonal symmetry with the space group *R*-3*m* and long-range AFM order below 20 K. They also found static internal fields below 20 K and short-range spin correlations below 35 K.[17] First-principle calculations indicate that BMTO is a spin gapless semiconductor that can be tuned to semiconductor or half-metal under strain.[18] High spin polarization, frustrated magnetic lattice, and tunable magnetic properties make BMTO

Received: March 4, 2024
Revised: June 6, 2024
Accepted: June 10, 2024
Published: June 25, 2024

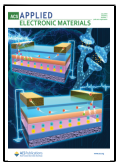

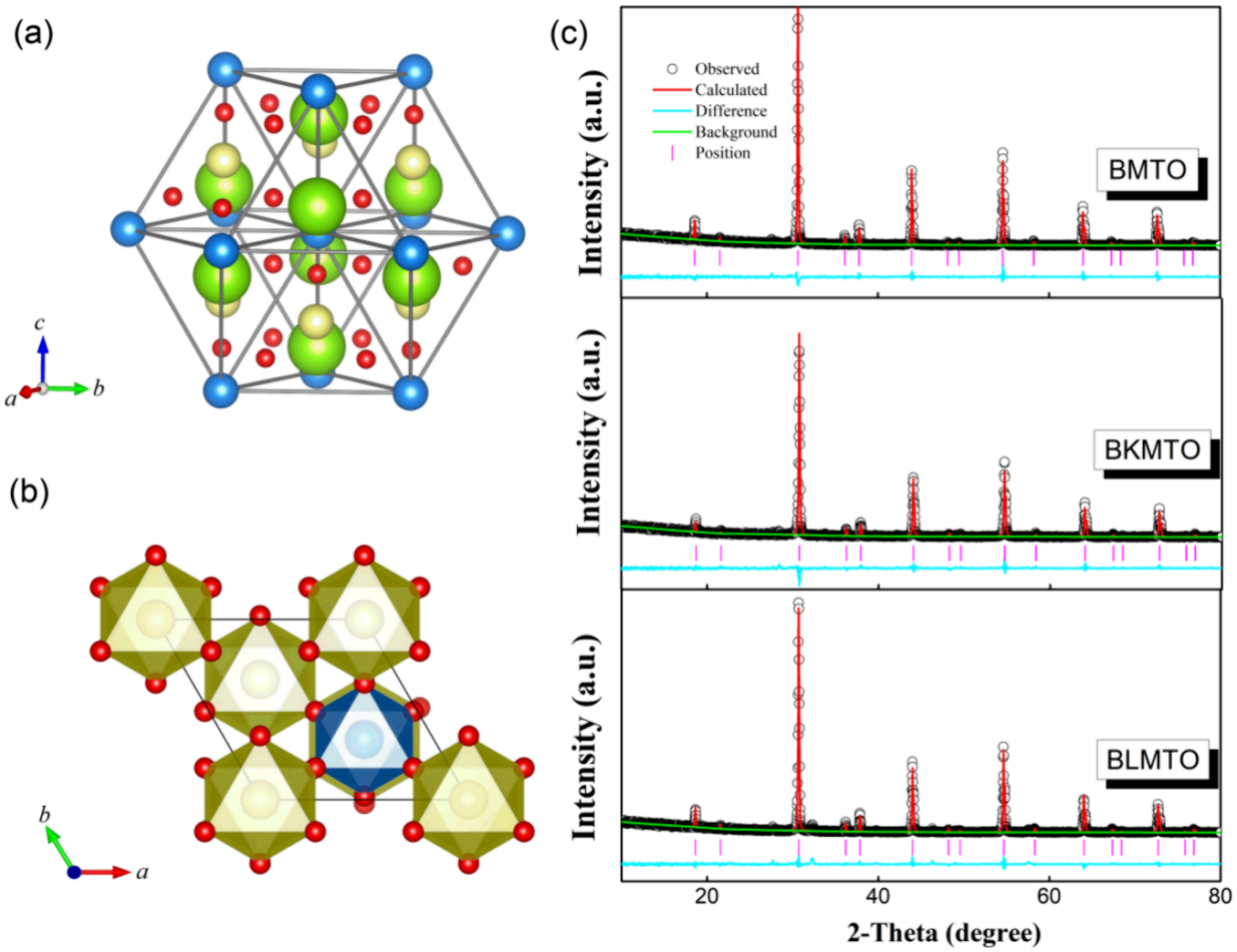

Figure 1. Crystal structure of double perovskites BMTO. Yellow, blue, green, and red atoms denote Ba, Mn, Te, and O, respectively. (a) Side view; (b) top view. (c) Rietveld refinement of PXD patterns for BMTO, BKMTO, and BLMTO taken at room temperature. The black marks are experimental values. The purple vertical bars point to locations of the Bragg diffractions; the blue lines are differences between the calculated and the experimental value. The red and green lines denote the calculated value and background.

a promising candidate for applications in spintronics and other types of devices.

In this work, we investigate physical properties of BMTO and K^+/La^{3+} ion-doped BMTO, i.e., $(Ba_{0.9}K_{0.1})_2MnTeO_6$ (BKMTO) and $(Ba_{0.9}La_{0.1})_2MnTeO_6$ (BLMTO), by powder X-ray diffraction (PXD), X-ray photoelectron spectroscopy (XPS), specific heat, and magnetic measurements. In Ba_2MnTeO_6, a magnetic transition is observed at ∼20 K, in agreement with previous reports.[15−17] K^+/La^{3+} ion doping tunes the valence state of the Mn ion, introducing oxygen vacancies and adsorptions. Unlike the antiferromagnetism of BMTO and BKMTO, BLMTO exhibits superparamagnetic behavior. In addition, density functional theory (DFT) calculations demonstrate all compounds are inclined to AFM coupling with a type III AFM ground state. The superparamagnetism of BLMTO originates from adsorbed oxygen ions due to La^{3+} doping.

EXPERIMENTAL AND CALCULATION SECTION

Sample Synthesis and Characterization. Polycrystalline BMTO, BKMTO, and BLMTO have been synthesized by the solid-state reaction method.[19−21] Selected raw materials including barium carbonate ($BaCO_3$, 99.99%), manganese dioxide (MnO_2, 99.99%), tellurium dioxide (TeO_2, 99.99%), potassium carbonate (K_2CO_3, 99.99%), and lanthanum trioxide (La_2O_3, 99.99%) were weighed according to the molar ratio and fully ground with acetone. It is worth noting that a 20% excess of the alkali carbonate is necessary to compensate for the loss due to volatilization. Other reagents were used in the stoichiometric amounts. Subsequently, the uniformly mixed samples were pressed into 13 mm diameter and 1 mm thick wafers by a tablet press. The pressed samples were then placed in an aluminum trioxide crucible and calcined in a high-temperature box furnace. After sintering at 1100 °C for 72 h, the samples were naturally cooled to room temperature. Brown polycrystalline ceramic samples were obtained.

Crystal structures of the samples have been characterized by PXD. PXD was measured by a Rigaku Smartlab3 (40 kV, 30 mA) in Bragg−Brentano reflection geometry with Cu Kα radiation (λ = 1.5406 Å), controlled by DIFFRACT Plus software. Testing range 2θ is from 10° to 80° with a scanning step of 0.01°. The PXD data have been refined by means of the Rietveld method, with the GSASII program.[22] Morphology images of the three samples were observed by scanning electron microscopy (SEM, FEI Inspect F50).

XPS, Magnetic, and Heat Capacity Measurements. XPS was utilized to detect the chemical bonding energy of elements and valence states of BMTO, BKMTO, and BLMTO samples. Magnetic susceptibility measurements were carried out using Quantum Design

https://doi.org/10.1021/acsaelm.4c00401
ACS Appl. Electron. Mater. 2024, 6, 4903−4911

MPMS3. Temperature-dependent magnetic susceptibility was tested between 5 and 300 K under field cooling (FC) and zero field cooling (ZFC) sequences in an applied field of 500 Oe. Hysteresis loops were obtained at different temperatures under an applied magnetic field that varied from −2 to 2 T. The curve of heat capacity with increasing temperature was measured with the heat capacity option of a Physical Property Measurement System (PPMS5, Quantum Design).

Theoretical Calculations. DFT calculations have been performed using the Vienna ab initio Simulation Package (VASP).[23,24] PBEsol pseudopotentials with Ba 5*d*, 6*p*, and 6*s*; Mn 3*d*, 3*p*, and 3*s*; Te 5*p*, 5*s*; and O 2*p* and 2*s* valence electrons were adopted.[25] The projector-augmented wave (PAW) potential with generalized gradient approximation was utilized with a cutoff energy of 500 eV.[26] The GGA+*U* method was applied to approximate electronic correlation in the Mn's *d*-orbitals.[27] The energy convergence criterion was 10^{-6} eV, and the criterion of the Hellmann−Feynman force was less than 0.01 eV/Å. The Monkhorst−Pack scheme is chosen to sample the Brillouin zone,[28] with a 6 × 3 × 3 *k*-point grid for the primitive cell. To mimic the La-doping and K-doping effects for BMTO, we perform carrier-doping calculations implemented by Virtual Crystal Approximation (VCA).

Monte Carlo (MC) simulations have been performed by the Markov-chain method with the Metropolis algorithm.[29] A 12 × 12 × 12 cubic lattice with periodic boundary conditions was adopted in the MC simulations, and a quenching process was used to avoid trapping into local potential minima due to nonequilibrium behavior. The initial 1×10^5 MC steps were discarded for thermal equilibrium, and another 1×10^5 MC steps were retained for statistical average in the simulation. The specific heat *C* was also calculated to determine the Néel temperature, T_N.

RESULTS AND DISCUSSION

There are two space groups of BMTO, including the trigonal phase (*R*-3*m*) and cubic phase (*Fm*-3*m*), which have been proposed. The calculated Goldschmidt tolerance factor of BMTO is $t \approx 1.034$, slightly bigger than 1, indicating a trigonal space group.[8] Besides, the *R*-3*m* space group allows for an additional degree of freedom for the positions of Ba and O sites along the *c*-axis. Here, we adopt the trigonal phase model. Both Mn^{2+} and Te^{6+} cations occupy the octahedral center site, forming a three-dimensional network by sharing oxygen ions. The Mn and Te ions, caged in an O_6 octahedron, are arranged alternately along the *a* direction, as shown in Figure 1a,b. The Ba atoms are surrounded by four MnO_6 or TeO_6 octahedra, and two types of coordination environments are in an alternative arrangement. As summarized in Table 1, the calculated lattice parameters ($a = b = 5.817$ Å, $c = 14.244$ Å) are in accordance with those of a previous experimental result ($a = b = 5.816$ Å, $c = 14.243$ Å). Ba, Mn, Te, and O atoms are placed at the Wyckoff 6c (0, 0, 0.25), 3b (0, 0, 0.5), 3a (0, 0, 0), and 18h (0.823, 0.646, and 0.912) sites, respectively.[30]

Table 1. Lattice Parameters and Atomic Coordinates of Calculation and Experimental Results for Ba_2MnTeO_6

	Lattice Parameters						
	a/Å	*b*/Å	*c*/Å	*α*/deg	*β*/deg	*γ*/deg	Volume/Å^3
Calcd	5.817	5.817	14.244	90	90	120	417.41
Exptl	5.816	5.816	14.243	90	90	120	417.23
	Atomic Coordinates						
	Atom	Site	Symmetry	*x*	*y*	*z*	Occ
Cal	Ba	6c	3*m*	0.0	0.0	0.25	1.0
	Mn	3b	−3*m*	0.0	0.0	0.5	1.0
	Te	3a	−3*m*	0.0	0.0	0.0	1.0
	O	18h	*m*	0.823	0.646	0.912	1.0
Exp	Ba	6c	3*m*	0.0	0.0	0.248	1.0
	Mn	3b	−3*m*	0.0	0.0	0.5	1.0
	Te	3a	−3*m*	0.0	0.0	0.0	1.0
	O	18h	*m*	0.848	0.697	0.912	1.0

To accurately determine the crystal structure, ambient-temperature PXD patterns of BMTO, BKMTO, and BLMTO were measured. Noticeable crystalline peaks can be indexed by the *R*-3*m* space group at 2θ = 18.6°(101), 21.58°(012), 30.71°(110), 36.18°(113), 37.85°(202), 43.99°(024), and so forth (Figure S1 in Supporting Information (SI)). PXD patterns do not show any trace of impurities from K- or La-related materials. Susceptibilities demonstrate a transition at 45 K, indicating the existence of Mn_3O_4, which will be discussed later. Rietveld refinement of three double perovskites processed by the GSAS II[22] software package is displayed in Figure 1c. For BKMTO and BLMTO, the diffraction peaks are not significantly different from those of BMTO, suggesting that they form a stable phase after implantation of K^+/La^{3+} ions. The lattice parameters and atomic coordinates of the refinement results for BLMTO and BKMTO at ambient temperature are similar to those for BMTO and are illustrated in Table 2. Refinement parameters including isotropic thermal factor (U_{iso}), *R*-factor (R_p), weighted profile *R*-factor (R_{wp}), and reduced chi square (χ^2) are listed in SI as Table S2. The interatomic distances and bond angles are illustrated in SI as Table S1. The interatomic distances and bond angles are illustrated in Table S1. Lattice parameters derived from DFT calculations are also listed for comparison. The details of the calculations will be discussed below. The surface topographies were characterized by SEM [Figure S2(a−f)], which reveal all samples consist of densely packed particles. The sizes of the particles are approximately 1 μm.

The XPS for the three polycrystalline samples in Figure 2 is employed to investigate the valence state variation. For Te^{6+} and Ba^{2+} cations, there is no shift of peaks, as shown in Figure 2a,b, indicative of the stable valence states. The peaks centered at 575.38 and 585.88 eV can be fitted by a single spin−orbit doublet, such as $3d_{5/2}$ and $3d_{3/2}$ for Te^{6+}. Their spin−orbit separation is around 10.5 eV. Analogously, the Ba−O binding energies are 778.68 and 793.98,eV, corresponding to single spin−orbit doublets of Ba^{2+}as $3d_{5/2}$ and $3d_{3/2}$, respectively.

O 1s spectra for three compositions can be deconvoluted to two or three peaks: the peaks of the O lattice (O_{lat}), oxygen vacancies (O_{vac}), and oxygen chemical adsorption (O_{ads}) were centered at 529.2, 531, and 533.1 eV, respectively, in line with ZnO nanorods reported by Chang et al.[31] The spectrum of the parent compound BMTO reveals a major peak of O_{lat} and a minor peak of O_{vac}. K^+ doping on the Ba site increased the area ratio of the O_{vac}/O_{lat}, indicating that K^{1+} substitution on the Ba^{2+} site introduces oxygen vacancies, possibly by the formation of surface defects. On the contrary, the spectrum of La^{3+} adulteration composition (BLMTO) exhibits three bulges and can be deconvoluted to three peaks corresponding to O_{lat}, O_{vac}, and O_{ads}. It is widely known that XPS is a surface-sensitive technology. The area ratios of O_{ads}/O_{lat} obviously enhanced, deriving from the formation of various surface defects and interrelated adsorption of many species (O_2, H_2O, CO_2, etc.) in ambient temperature, as shown in Figure 2c.

From Figure 2d, Mn 2*p* spectra for three compositions demonstrate spin−orbit doublets of Mn $2p_{1/2}$ and Mn $2p_{3/2}$ with a binding energy gap of 11.7 eV. The peaks located at

https://doi.org/10.1021/acsaelm.4c00401
ACS Appl. Electron. Mater. 2024, 6, 4903−4911

Table 2. Lattice Parameters and Atomic Coordinates of Refinement Results for $(Ba_{0.9}La_{0.1})_2MnTeO_6$ and $(Ba_{0.9}K_{0.1})_2MnTeO_6$ at 300 K

	Lattice Parameters						
	a/Å	*b*/Å	*c*/Å	*α*/deg	*β*/deg	*γ*/deg	Volume/Å^3
$(Ba_{0.9}La_{0.1})_2MnTeO_6$	5.816	5.816	14.252	90	90	120	417.57
$(Ba_{0.9}K_{0.1})_2MnTeO_6$	5.814	5.814	14.235	90	90	120	416.85
	Atomic Coordinates						
	Atom	Site	Symmetry	*x*	*y*	*z*	Occ
EXP $(Ba_{0.9}La_{0.1})_2MnTeO_6$	Ba	6c	3*m*	0.0	0.0	0.250	0.9
	Mn	3b	−3*m*	0.0	0.0	0.5	1.0
	Te	3a	−3*m*	0.0	0.0	0.0	1.0
	O	18h	*m*	0.854	0.708	0.900	1.0
	La	6c	3*m*	0.0	0.0	0.2501	0.1
EXP $(Ba_{0.9}K_{0.1})_2MnTeO_6$	Ba	6c	3*m*	0.0	0.0	0.249	0.9
	Mn	3b	−3*m*	0.0	0.0	0.5	1.0
	Te	3a	−3*m*	0.0	0.0	0.0	1.0
	O	18h	*m*	0.827	0.6541	0.9134	1.0
	K	6c	3*m*	0.0	0.0	0.249	0.1

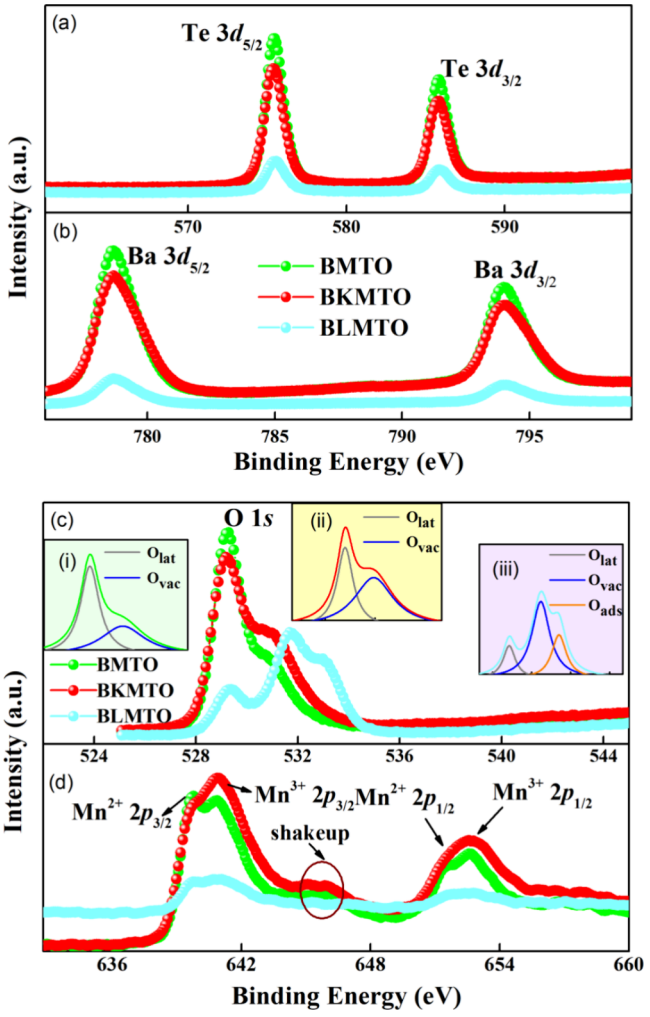

Figure 2. High-resolution XPS of (a) Te 3*d*, (b) Ba 3*d*, (c) O 1*s*, and (d) Mn 2*p*. (i−iii) show that the spectra are deconvoluted to two or three specific peaks, including oxygen lattice, oxygen vacancy, and oxygen adsorption, which are marked by gray, blue, and orange lines, respectively. The vibration areas (satellite peaks) are indicated by a red circle.

639.7 eV/651.4 eV and 640.8 eV/652.6 eV are assigned to be $2p_{1/2}$ and $2p_{3/2}$ for 2+ and 3+ valence states of Mn, respectively. For BKMTO, peaks corresponding to Mn^{3+} were obviously enhanced. There are satellite peaks on the higher binding energy (lower kinetic energy) region of Mn 2*p* in XPS, coming from the charge transfer from the outer electron shell to an unoccupied orbit during the photoelectron process.[32,33] Theoretically, substitution of K^+/La^{3+} on the Ba^{2+} site will introduce hole/electron doping, respectively. The valence state of Mn should be modified correspondingly. However, XPS results show that part of the doping is neutralized by oxygen deficiency or oxygen adsorption.

The magnetic properties of all samples are adequately investigated by DC magnetometry, as exhibited in Figure 3a−c. The temperature-dependent magnetic susceptibilities are measured with a magnetic field of 500 Oe under both ZFC and FC sequences. The ZFC curve of BMTO displays two phase transitions at ∼20 and 45 K, suggesting AFM and ferro/ferrimagnetic transitions, respectively.[14,15] The transition at 45 K for which the FC curve deviates from the ZFC curve should be attributed to a paramagnetic to ferromagnetic (FM) transition of impurity phase Mn_3O_4, in agreement with previous reports on BMTO[16] and other compounds such as Sr_2MnTeO_6[34] and $Mn_4Ta_2O_9$.[35] The Mn_3O_4 phase can not be detected by powder XRD measurement, indicating the tiny proportion of this impurity phase. However, its FM signal is more pronounced in a low field DC susceptibility measurement. Both ZFC and FC curves present a small kink at ∼20 K, resulting from intrinsic AFM order of BMTO.

As illustrated in Figure 3d, the reciprocal magnetic susceptibility $(1/\chi)$ of BMTO is fitted by the Curie−Weiss law: $\chi = \chi_0 + C/(T - \theta_{CW})$, where χ_0 is the contribution from diamagnetism and Van Vleck paramagnetism, C is the Curie constant, and θ_{CW} *is* the paramagnetic Curie temperature. The temperature range of fitting is between 50 and 350 K yields, C = 5.1 emu K mol^{-1}, θ_{CW} = −158 K, and χ_0 is negligible. The negative paramagnetic Curie temperature denotes that the exchange interaction for BMTO is mainly AFM. The effective moment is assessed to be $\mu_{eff} = (8C)^{1/2}$ = 6.33 μ_B, larger than the expected one, 5.91 μ_B (S = 5/2), for high-spin Mn^{2+}.

Magnetic properties of K^+/La^{3+}-doped BMTO are measured under the same conditions. The susceptibility curves of

https://doi.org/10.1021/acsaelm.4c00401
ACS Appl. Electron. Mater. 2024, 6, 4903−4911

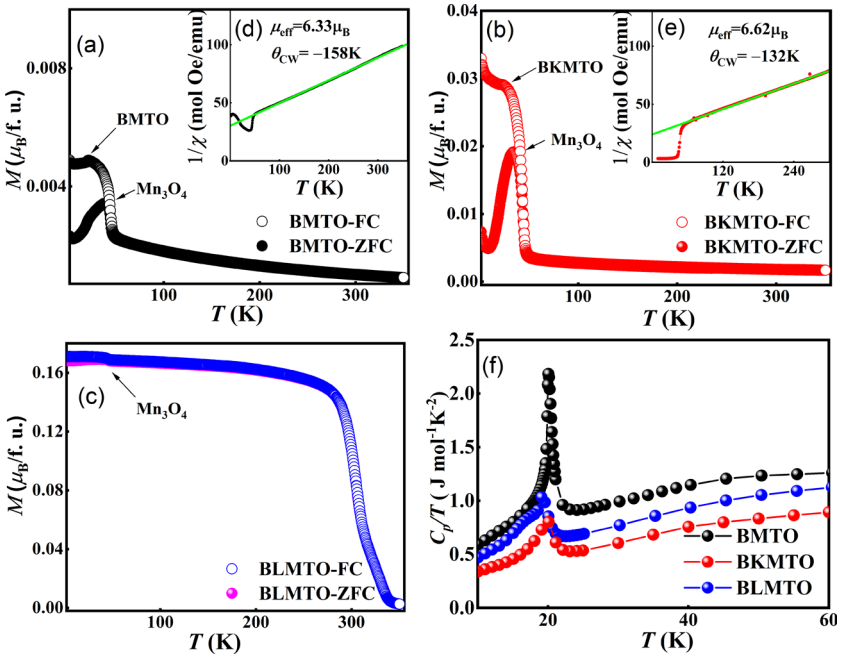

Figure 3. (a–c) Susceptibility vs temperature of three ceramics measured at 500 Oe. (d, e) Inverse of the susceptibility fitted to the Curie–Weiss law. (f) The temperature dependence of specific heat capacity (C_p) of three polycrystalline samples in the temperature range 2 K ≤ T ≤ 60 K at the ZFC state.

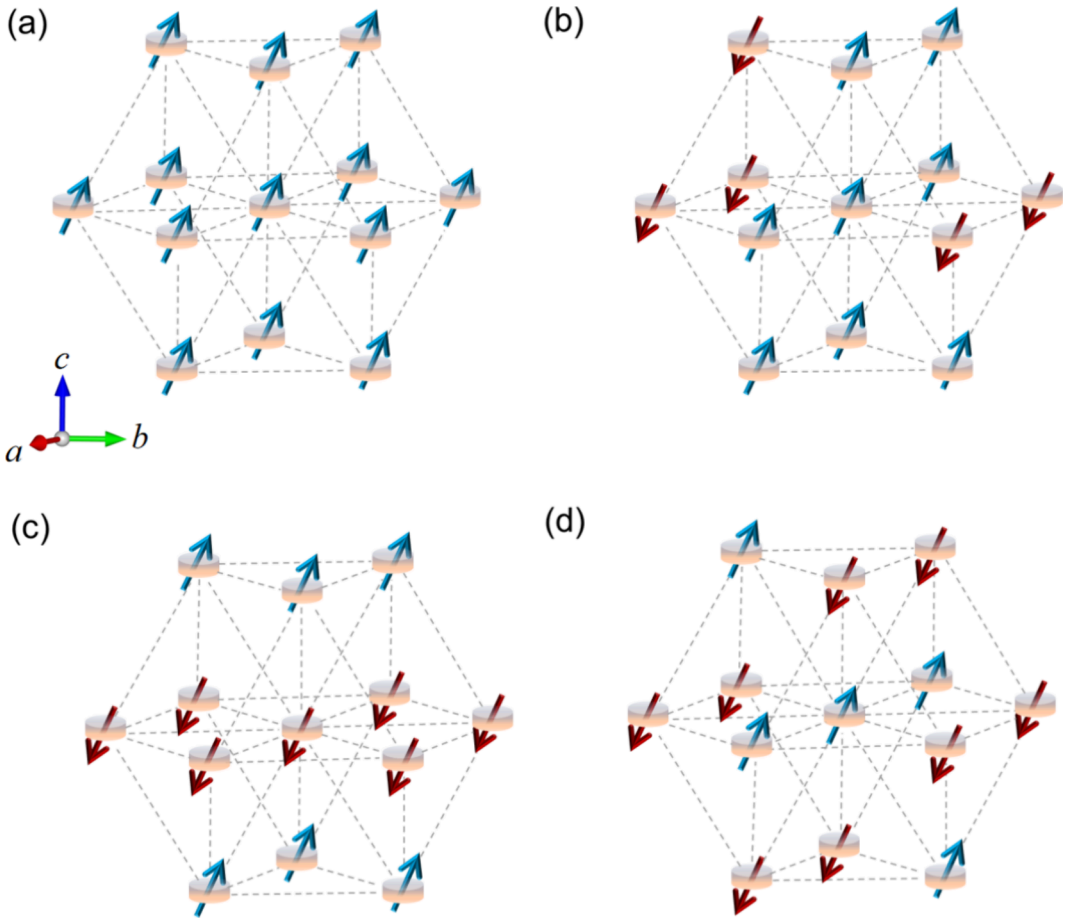

Figure 4. Four possible magnetic orders of triangular-phase BMTO: (a) FM, (b) type I AFM, (c) type II AFM, and (d) type III AFM. The upper and lower magnetic sequence directions are denoted by red and blue arrows, respectively.

https://doi.org/10.1021/acsaelm.4c00401
ACS Appl. Electron. Mater. 2024, 6, 4903–4911

BKMTO are similar to those of BMTO. The FC curve deviates from the ZFC curve at ∼40 K, which is attributed to the paramagnetic to ferromagnetic transition of impurity phase Mn_3O_4. This transition is more pronounced in BKMTO than in BMTO, indicating an increased percentage of Mn_3O_4 impurities. A kink at ∼20 K is only observed in the FC curve. CW fitting of BKMTO yields $\theta_{CW} = -132$ K and $\mu_{eff} = 6.62\ \mu_B$. Distinct from those of BMTO and BKMTO, the ZFC and FC curves for BLMTO almost coincide, showing an obvious superparamagnetic/ferromagnetic behavior below room temperature. Further field-dependent magnetization (MH) curves at various temperatures are duplicated in Figure S3 of the SI. MH curves for the pristine compound BMTO show neither hysteresis nor remanence, indicating the absence of ferromagnetism. But for BKMTO (Figure S3b in the SI), a small opened-up hysteresis loop can be captured at low temperature. K dopants may introduce more Mn_3O_4 impurities or other types of impurities, resulting in the existence of weak ferromagnetism. MH curves of BLMTO show typical behavior of superparamagnetism below 350 K.

The temperature-dependent specific heats (C_p) of three compositions are measured in the temperature range 2 K ≤ T ≤ 60 K, as shown in Figure 3e. Apparent λ-like peaks at about 20 K can be observed in all compositions, verifying the existence of the AFM long-range order in the major phase, while a transition peak observed in the $M-T$ curve at 45 K from Mn_3O_4 impurity disappeared, resulting from an imperceptible change in the whole entropy.

Magnetic properties of the BMTO are also studied theoretically via DFT calculations and MC simulations. Four probable magnetic structures are considered, including FM and three types of AFM order (types I, II, III, as seen in Figure 4). The energy difference of these magnetic orders obtained by our DFT calculation is shown in Table 3, indicating that the type III AFM order is always the ground state for different results introducing on-site Coulomb $U_{eff} = 3$ and 4 eV; for the following analysis we adopted $U_{eff} = 4$ eV. The magnetic state named "type III AFM" is in accordance with the stripe-type AFM with a propagation vector k = (0.5, 0.5, 0) in previous reports.[15−17] In addition, the spin−orbit coupling is involved in considering the magnetic anisotropy.

Table 3. Total Energies (in units of meV) per f.c. with Various Magnetic Orders under Different On-Site Coulomb U_{eff} and with 2% Electron/Hole per f.c. (Denoted by 2% *e* or 2% *h*)[a]

	FM	Type I AFM	Type II AFM	Type III AFM
U_{eff} = 3 eV	0	−33.37	−33.33	−47.05
U_{eff} = 4 eV	0	−32.32	−32.80	−41.74
2% *e* (U_{eff} = 4 eV)	0	−17.21	−17.31	−27.49
2% *h* (U_{eff} = 4 eV)	0	−17.45	−17.49	−39.86

[a]The energy of FM order is set as the reference.

A Heisenberg model is introduced including the nearest-neighbor J_1 (along different directions by neglecting their tiny differences), next-nearest-neighbor J_2, and magnetic anisotropy A:

$$H = J_1 \sum_{i,j} S_i S_j + J_2 \sum_{i,j} S_i S_j + A \sum_i (S_i^z)^2 \quad (1)$$

To extract all exchange coefficients, first, we performed a calculation of maximally localized Wannier functions (MLWFs) by Wannier90 code postprocessing from DFT results.[36] Calculated by a tight-binding model with bases of Wannier functions, the band structure compared with the DFT result is plotted in Figure 5a, which is in good agreement. Next, we introduced a green function method utilizing TB2J code,[37] to directly calculate the exchange interaction decomposed as separate contributions from each pair of orbitals (WF bases) by

$$J_{ij}^{nm} = -\frac{1}{4\pi}\mathrm{Im}\int_{-\infty}^{E_f} \Delta_i^n G_{in,jm}^{\uparrow} \Delta_j^m G_{in,jm}^{\downarrow}\, d\epsilon \quad (2)$$

where n, m denote the indexes of Mn 3d orbitals including d_{z^2}, d_{xz}, d_{yz}, d_{xy}, and $d_{x^2-y^2}$. Accordingly, J_1 and J_2 are written as the matrixes:

$$J_1 = \begin{bmatrix} 0.32 & 0 & 0 & 0.04 & 0 \\ 0 & 0 & 0 & 0 & 0 \\ 0 & 0 & 0.01 & 0 & 0 \\ 0.04 & 0 & 0 & 0.1 & 0 \\ 0 & 0 & 0 & 0 & 2.46 \end{bmatrix} \quad (3)$$

$$J_2 = \begin{bmatrix} -0.03 & 0 & 0 & 0 & 0 \\ 0 & 0 & 0 & 0 & 0 \\ 0 & 0 & 0 & 0 & 0 \\ 0 & 0 & 0 & 0 & 0 \\ 0 & 0 & 0 & 0 & -0.39 \end{bmatrix} \quad (4)$$

An AFM J_1 is expected since the half-filling orbitals prefer the AFM coupling according to the Goodenough−Kanamori rule.[38,39] As for the next-nearest-neighbor exchange, mostly their d_{x^2} orbitals contribute to unexpected FM interaction. A strong hybridization occurs between 5sp^3 orbitals of the Te atom and 2p orbitals of the O atom, producing hybrid orbitals that stayed at the deep energy level, as shown in Figure 5a. The partial charge density of the isolated hybrid orbitals is plotted in Figure 5d. Within the indirect Mn−O−Te−O-Mn path, the 5sp^3−2p hybrid orbitals induce hopping from electrons with the same spin between two adjacent O atoms, which provides a relatively weak FM superexchange interaction.

Taking account of the contribution of all the orbitals, we obtain AFM J_1 = 2.95 meV and FM J_2 = −0.42 meV as illustrated in Figure 5b. Besides, by constraining the spin direction in the DFT calculation involving spin−orbit coupling, we obtain a weak magnetic anisotropy A = 0.02 meV. In our MC simulation, a sharp peak of specific heat indicates the Néel temperature T_N = 28 K (Figure 5c), which is very consistent with our susceptibility data. As listed in Table 3, in electron/hole-doping cases, the type-III AFM is still the ground state, but the energy differences between various magnetic orders are rather smaller. The exchange coefficients being extracted are AFM J_1 = 2.91 meV and FM J_2 = −0.23 meV for electron-doping (2% per f.c.) and AFM J_1 = 2.94 meV and FM J_2 = −0.26 meV for hole-doping (2% per f.c.). As we can expect, the Néel temperature for electron/hole-doping BMTO would be slightly reduced compared with BMTO, as shown in Figure 5c, owing to the significant reduction of J_2.

Our DFT calculations and MC simulations agree well with the experimental results of BKMTO. The superparamagnetism reflected by magnetic measurements in BLMTO is surprising. It may be related to the oxygen chemical adsorption at surface as evidenced by XPS. A previous study showed that adsorbed

https://doi.org/10.1021/acsaelm.4c00401
ACS Appl. Electron. Mater. 2024, 6, 4903−4911

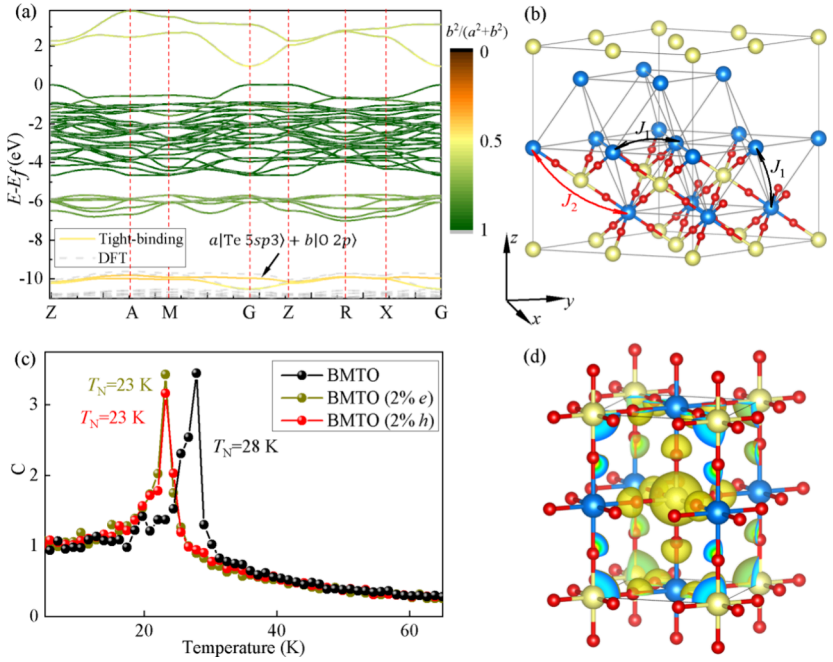

Figure 5. (a) Band structures obtained by fitting of Wannier functions with the tight-binding model (solid lines), compared with DFT (dashed lines). (b) The nearest-neighbor exchange J_1 and next-nearest-neighbor exchange J_2. (c) Specific heat with varying temperature in MC simulations. (d) Partial density plotted within the energy $E-E_f$ range [−10.6, 9] corresponding to the $5sp^3-2p$ hybridization orbitals.

oxygen at the surface of undoped ZnO nanorods is responsible for the superparamagnetism in the samples.[40] At the surface of samples, adsorbed oxygen may depart from the −2 valence state and become a magnetic particle. Particle size and surface defects have a profound influence on the macromagnetism. A similar phenomena may happen in our system. The room-temperature superparamagnetism may be useful for biomedicine fields such as magnetic resonance imaging and magnetic hyperthermia of tumors.

CONCLUSION

The structural, magnetic, and electronic properties of the *B*-site rock salt type ordered double perovskite Ba_2MnTeO_6, as well as the K^+/La^{3+}-doped compositions, have been investigated both experimentally and theoretically. They possess a trigonal *R*-3*m* structure with $a = b \sim 5.81$ Å at ambient temperature. Specific heat measurements indicate that all compounds undergo phase transitions at ∼20 K. Magnetic measurements demonstrate that these transitions in parent compound Ba_2MnTeO_6 and $(Ba_{0.9}K_{0.1})_2MnTeO_6$ are paramagnetic to AFM phase transitions. However, magnetic measurements indicate that $(Ba_{0.9}La_{0.1})_2MnTeO_6$ exhibits a superparamagnetic behavior below room temperature. The superparamagnetism may originate from adsorbed oxygen ions at the surface, as suggested by XPS. The magnetic structure in the ordered state is investigated by DFT calculations, which prefer a type III AFM order with $T_N \sim 20$ K based on the Monte Carlo simulations, in agreement with experimental conclusions. Further study on atmosphere treated samples should be performed to explore the origin of the room-temperature superparamagnetism in $(Ba_{0.9}La_{0.1})_2MnTeO_6$, which could be a candidate functional material with potential applications. This work also guides the way to manipulate the magnetism of double perovskite via ion implantation.

ASSOCIATED CONTENT

Supporting Information

The Supporting Information is available free of charge at https://pubs.acs.org/doi/10.1021/acsaelm.4c00401.

More information about Rietveld refinement results including XRD pattern of BMTO with *hkl* labeling; isotropic thermal factor (U_{iso}), *R*-factor (R_p), weighted profile *R*-factor (R_{wp}), and reduced chi square (χ^2); bond distances and bond angles; SEM images of three ceramics; isothermal magnetizations measured at different temperatures of BMTO, BKMTO, and BLMTO (PDF)

AUTHOR INFORMATION

Corresponding Authors

Jun Chen − *Key Laboratory of Quantum Materials and Devices of Ministry of Education, School of Physics, Southeast University, Nanjing 211189, China*; Email: jpakech@seu.edu.cn

Jin Peng − *Key Laboratory of Quantum Materials and Devices of Ministry of Education, School of Physics, Southeast University, Nanjing 211189, China*; orcid.org/0000-0001-8863-2640; Email: jpeng@seu.edu.cn

Authors

Haipeng You − *School of Sciences, Changzhou Institute of Technology, Changzhou 213032, China*

Yixiao Chen − *School of Sciences, Changzhou Institute of Technology, Changzhou 213032, China*

Yue Li − *School of Sciences, Changzhou Institute of Technology, Changzhou 213032, China*

Xiyu Chen − *Key Laboratory of Quantum Materials and Devices of Ministry of Education, School of Physics, Southeast University, Nanjing 211189, China; Hubei Key Laboratory of Photoelectric Materials and Devices, School of Materials*

https://doi.org/10.1021/acsaelm.4c00401
ACS Appl. Electron. Mater. 2024, 6, 4903−4911

Science and Engineering, Hubei Normal University, Huangshi 435002, China; orcid.org/0000-0002-8702-5491

Meifeng Liu − *Hubei Key Laboratory of Photoelectric Materials and Devices, School of Materials Science and Engineering, Hubei Normal University, Huangshi 435002, China;* orcid.org/0000-0001-5733-8764

Shuai Dong − *Key Laboratory of Quantum Materials and Devices of Ministry of Education, School of Physics, Southeast University, Nanjing 211189, China;* orcid.org/0000-0002-6910-6319

Complete contact information is available at: https://pubs.acs.org/10.1021/acsaelm.4c00401

Notes

The authors declare no competing financial interest.

■ ACKNOWLEDGMENTS

The work at Southeast University was supported by the National Natural Science Foundation of China (Grant No. 52130706). Work at Changzhou Institute of Technology was supported by the Natural Science Foundation of Universities of Jiangsu Province of China (23KJB140001) and Jiangsu Province College Students' Platform for innovation and entrepreneurship training program (202311055013Z). Work at Hubei Normal University was supported by the National Natural Science Foundation of China (12074111 & 52272108).

■ REFERENCES

(1) Bednorz, J. G.; Müller, K. A. Possible high T_C superconductivity in the Ba-La-Cu-O system. *Phys. B Condens. Matter* **1986**, *64*, 189−193.

(2) Dong, S.; Liu, J.-M.; Cheong, S.-W.; Ren, Z. F. Multiferroic materials and magnetoelectric physics: symmetry, entanglement, excitation, and topology. *Adv. Phys.* **2015**, *64*, 519.

(3) Pickett, W.; Singh, D. J. Chemical disorder and charge transport in ferromagnetic manganites. *Phys. Rev. B* **1997**, *55*, R8642.

(4) Fiebig, M. Revival of the Magnetoelectric Effect. *J. Phys. D: Appl. Phys.* **2005**, *38*, R123.

(5) Dong, S.; Yu, R.; Yunoki, S.; Liu, J.-M.; Dagotto, E. Ferromagnetic tendency at the surface of CE-type charge-ordered manganites. *Phys. Rev. B* **2008**, *78*, 064414.

(6) Cheong, S.-W.; Mostovoy, M. Multiferroics: a magnetic twist for ferroelectricity. *Nat. Mater.* **2007**, *6*, 13−20.

(7) Ramesh, R.; Spaldin, N. Multiferroics: progress and prospects in thin films. *Nat. Mater.* **2007**, *6*, 21−29.

(8) Vasala, S.; Karppinen, M. $A_2B'B''O_6$ perovskites: a review. *Prog. Solid State Chem.* **2015**, *43*, 1−36.

(9) Pilania, G.; Mannodi-Kanakkithodi, A.; Uberuaga, B. P.; Ramprasad, R.; Gubernatis, J. E.; Gubernatis, J. E.; Lookman, T. Machine learning bandgaps of double perovskites. *Sci. Rep.* **2016**, *6*, 19375.

(10) Winiarski, M. J.; Deren, P. Electronic structure of $A_2B'B''O_6$-type (A = Ca, Sr, Ba; B'=Mg, Zn; B''=Mo, W) double perovskite oxides. *Opt. Mater.* **2019**, *90*, 95−98.

(11) Briones, J.; Guinto, M. C.; Pelicano, C. M. Accelerated lattice constant prediction perovskite materials (ABX3, $A_2B'B''O_6$) using partial least squares and principal component regression methods. *Mater. Lett.* **2021**, *298*, 130040.

(12) Chen, X. Y.; Xu, J.; Xu, Y. S.; Luo, F.; Du, Y. P. Rare earth double perovskites: a fertile soil in the field of perovsite oxides. *Inorg. Chem. Front.* **2019**, *6*, 2226−2238.

(13) Wulff, L.; Wedel, B.; Müller-Buschbaum, H. Zur Kristallchemie von Telluraten mit Mn^{2+} imkationsichen und anionischen Teil der KristallstruKtur: $(Mn_{2.4}Cu_{0.6})TeO_6$, Ba_2MnTeO_6 and $(Mn_{0.5}Te_{0.5})O_3$. *Z. Naturforsch. B* **1998**, *53*, 49−52.

(14) Retuerto, M.; Skiadopoulou, S.; Li, M. R.; Abakumov, A. M.; Croft, M.; Ingatov, A.; Sarkar, T.; Abbertt, B. M.; Pokorny, J.; Savinov, M.; Nuzhuyy, D.; Prokleska, J.; Abeykoon, M.; Stephens, P. W.; Hodges, J. P.; Vanek, P.; Fennie, C. J.; Rabe, K. M.; Kamba, S.; Greenblatt, M. Pb_2MnTeO_6 Double Perovskite: An Antipolar Antiferromagnet. *Inorg. Chem.* **2016**, *55*, 4320−4329.

(15) Mustonen, O. H. J.; Pughe, C. E.; Walker, H. C.; Mutch, H. M.; Stenning, G. B. G.; Coomer, F. C.; Cussen, E. J. Diamagnetic *d*-orbitals drive magnetic structure selection in the double perovskite Ba_2MnTeO_6. *Chem. Mater.* **2020**, *32*, 7070−7079.

(16) Li, L. S.; Narayanan, N.; Jin, S. J.; Yu, J.; Liu, Z. J.; Sun, H. L.; Wang, C.-W.; Peterson, V. K.; Liu, Y.; Danikin, S.; Yao, D. X.; Yu, D. H.; Wang, M. Matertic ordering and spin dynamics in the $S = 5/2$ staggered triangular lattice antiferromagnet Ba_2MnTeO_6. *Phys. Rev. B* **2020**, *102*, 094413.

(17) Khatua, J.; Arh, T.; Mishra, S. B.; Luetkens, H.; Zorko, A.; Sana, B.; Rao, M. S. R.; Nanda, B. R. K.; Khuntia, P. Development of short and long-range magnetic order in the double perovskite based frustrated triangular lattice antiferromagnet Ba_2MnTeO_6. *Sci. Rep.* **2021**, *11*, 6959.

(18) Huang, H.-M.; Yu, Q.; Tong, R.; Wu, C.-R.; Zhu, Z.-W.; He, Z.-D.; Luo, S.-J. Transition of spin gapless semiconductor to semiconductor and half-metal in ferromagnetic Ba_2MnTeO_6. *Results Phys.* **2021**, *25*, 104315.

(19) Zhao, K.; Shen, Y.; He, F.; Huang, Z.; Wei, G. Q.; Zheng, A. Q.; Li, H. B.; Zhao, Z. L. Preparation of double perovskite-type oxide $LaSrFeCoO_6$ for chemical looping steam methane reforming to produce syngas and hydrogen. *J. Rare. Earth* **2016**, *34*, 1032−1041.

(20) Yang, X. M.; Wang, Y.; Jiang, J. J.; Li, M. M.; Tang, Z.; Cai, H. L.; Zhang, F. M.; Wu, X. S. Composition effects on structure and optical properties in double perovskite derivatives semiconductors $Cs_2SnI_{6-x}Br_x$ (x = 0−6). *APL Mater.* **2020**, *8*, 021102.

(21) Chen, X. Y.; Ding, N.; Liu, M. F.; Zou, T.; Garlea, V. O.; Gong, J. W.; Liu, F.; Xie, Y. L.; Yang, L.; Zheng, S. H.; Wang, X. Z.; Dong, S.; Charlton, T.; Liu, J.-M. Incommensurate-commensurate magnetic phase transition in double tungstate $Li_2Co(WO_4)_2$. *Chin. Phys. B* **2022**, *31*, 047501.

(22) Toby, B.; Dreele, R. B. V. GSAS-II: the gensis of a modern open-source all purpose crystallography software package. *J. Appl. Crystallogr.* **2013**, *46*, 544−549.

(23) Kresse, G.; Furthmullerüller, J. Efficiency of *ab-initio* total energy calculations for metals and semiconductors using a plane-wave basis set. *Comput. Mater. Sci.* **1996**, *6*, 15−50.

(24) Kresse, G.; Furthmullerüller, J. Efficient iterative schemes for *ab initio* total-energy calculations using a plane-wave basis set. *Phys. Rev. B* **1996**, *54*, 11169.

(25) Perdew, J. P.; Ruzsinszky, A.; Csonka, G. I.; Vydrov, O. A.; Scuseria, G. E.; Constantin, L. A.; Zhou, X.; Burke, K. Restoring the density-gradient expansion for exchange in solids and surface. *Phys. Rev. Lett.* **2008**, *100*, 136406.

(26) Perdew, J. P.; Burke, K.; Ernzerhof, M. Generalized gradient approximation made simple. *Phys. Rev. Lett.* **1997**, *78*, 1396.

(27) Liechtenstein, A. I.; Anisimov, V. I.; Zaanen, J. Denstiy-functional theory and strong interactions: orbital ordering in mott-hubbard insulators. *Phys. Rev. B* **1995**, *52*, R5467.

(28) Monkhorst, H. J.; Pack, J. D. Special points for Brillouin-zone integrations. *Phys. Rev. B* **1976**, *13*, 5188.

(29) Laudau, D.; Binder, K. *A Guide to Monte Carlo Simulations in Statistical Physics*; Cambrige University Press, Cambridge, 2021.

(30) Aroyo, M. I.; Kirov, A.; Capillas, C.; Perez-Mato, J.; Wondratschek, H. Bibao crystallographic server. II. Representations of crystallographic point groups and space groups. *Acta Crystallogr. A* **2006**, *62*, 115−128.

(31) Chang, F.-M.; Brahma, S.; Huang, J.-H.; Wu, Z.-Z.; Lo, K.-Y. Strong correlation between optical properties and mechanism in deficiency of normalized self-assembly ZnO nanorods. *Sci. Rep.* **2019**, *9*, 905.

(32) Kang, M.; Park, E. D.; Kim, J. M.; Yie, J. E. Manganese oxide catalysts for NO_x reduction with NH_3 at low temperature. *Appl. Catal., A* **2007**, *327*, 261−269.
(33) Iwanowski, R. J.; Heinonen, M. H.; Paszkowicz, W.; Minikaev, R.; Story, T.; Witkowska, B. X-ray photoelectron study of $Sn_{1-x}Mn_xTe$ semimagnetic semiconductors. *Appl. Surf. Sci.* **2006**, *252*, 3632−3641.
(34) Ortega-San Martin, L.; Chapman, J. P.; Lezama, L.; Sánchez Marcos, J.; Rodríguez-Fernández, J.; Arriortua, M. I.; Rojo, T. Magnetic properties of the ordered double perovskite Sr_2MnTeO_6. *Eur. J. Inorg. Chem.* **2006**, *7*, 1362−1370.
(35) Narayanan, N.; Senyshyn, A.; Mikhailova, D.; Faske, T.; Lu, T.; Liu, Z.; Weise, B.; Ehrenberg, H.; Mole, R. A.; Hutchison, W. D.; Fuess, H.; Mclntyre, G. J.; Liu, Y.; Yu, D. Magnetic structure and spin correlations in magnetoelectric honeycomb $Mn_4Ta_2O_9$. *Phys. Rev. B* **2018**, *98*, 134438.
(36) Pizzi, G.; Vitale, V.; Arita, R.; Blügel, S.; Freimuth, F.; Géranton, G.; Gibertini, G.; Gresch, D.; Johnson, D.; et al. Wannier90 as a community code: new features and applications. *J. Phys.: Condens. Matter.* **2020**, *32*, 165902.
(37) Hukushima, K.; Nemoto, K. Exchange Monte Carlo method and application to spin glass simulations. *J. Phys. Soc. Jpn.* **1996**, *65*, 1604.
(38) Goodenough, J. B. Theory of the role of covalence in the perovskite-type manganites[La, M(II)]MnO_3. *Phys. Rev. B* **1955**, *100*, 564.
(39) Kanamori, J. Crystal distortion in magnetic compounds. *J. Appl. Phys.* **1960**, *31*, S14−S23.
(40) Koshy, O.; Khadar, M. A. Superparamagnetism in undoped ZnO nanorods. *Appl. Sur. Sci.* **2015**, *346*, 528−533.

https://doi.org/10.1021/acsaelm.4c00401
ACS Appl. Electron. Mater. 2024, 6, 4903−4911